

Amplification of enstrophy in the far field of an axisymmetric turbulent jet

O. R. H. BUXTON[†] AND B. GANAPATHISUBRAMANI

Department of Aeronautics, Imperial College London,
Prince Consort Road, London SW7 2AZ, UK

(Received 10 July 2009; revised 7 December 2009; accepted 7 December 2009;
first published online 19 March 2010)

The amplification of enstrophy is explored using cinematographic stereoscopic particle image velocimetry data. The enstrophy production rate is investigated by observation of the statistical tendency of the vorticity vector ($\boldsymbol{\omega}$) to align with the eigenvectors of the rate of strain tensor (\boldsymbol{e}_i). Previous studies have shown that $\boldsymbol{\omega}$ preferentially aligns with the intermediate strain-rate eigenvector (\boldsymbol{e}_2) and is arbitrarily aligned with the extensive strain-rate eigenvector (\boldsymbol{e}_1). This study shows, however, that the nature of enstrophy amplification, whether it is positive (enstrophy production) or negative (enstrophy destruction), is dictated by the alignment between $\boldsymbol{\omega}$ and \boldsymbol{e}_1 . Parallel alignment leads to enstrophy production ($\omega_i S_{ij} \omega_j > 0$), whereas perpendicular alignment leads to enstrophy destruction ($\omega_i S_{ij} \omega_j < 0$). In this way, the arbitrary alignment between $\boldsymbol{\omega}$ and \boldsymbol{e}_1 is the summation of the effects of enstrophy producing and enstrophy destroying regions. The structure of enstrophy production is also examined with regards to the intermediate strain-rate eigenvalue, s_2 . Enstrophy producing regions are found to be topologically ‘sheet-forming’, due to an extensive (positive) value of s_2 in these regions, whereas enstrophy destroying regions are found to be ‘spotty’. Strong enstrophy producing regions are observed to occur in areas of strong local swirling as well as in highly dissipative regions. Instantaneous visualizations, produced from the volume of data created by Taylor’s hypothesis, reveal that these ‘sheet-like’ strong enstrophy producing regions encompass the high enstrophy, strongly swirling ‘worms’. These ‘worms’ induce high local strain fields leading to the formation of dissipation ‘sheets’, thereby revealing enstrophy production to be a complex interaction between rotation and strain – the skew-symmetric and symmetric components of the velocity gradient tensor, respectively.

1. Introduction

There is a great interest in examining the rate of strain tensor (S_{ij}) and rotation tensor (Ω_{ij}) fields, which are respectively the symmetric and skew symmetric parts of the velocity gradient tensor ($D_{ij} = \partial u_i / \partial x_j$). The relation between the strain rate and the rotation tends to be strongly non-local and may be only weakly correlated (Tsinober 2000). Also, kinetic energy dissipation, the ‘end result’ of the energy cascade, is directly associated with strain and not rotation. Importantly, however, vortex stretching/compression is essentially a process of the interaction between strain and rotation (Tsinober 2000; Hamlington, Schumacher & Dahm 2008). So important is this interaction that it has been described as ‘intrinsic to the very nature of

[†] Email address for correspondence: o.buxton07@imperial.ac.uk

three-dimensional turbulence' (Tennekes & Lumley 1972; Bermejo-Moreno, Pullin & Horiuti 2009). Both rate of strain and rotation appear in the equations governing the dynamics of each other, suggesting that the effects of the two fields cannot be decoupled. Equations (1.1) and (1.2) illustrate this fact. The strain-rate tensor (S_{ij}) features in the production term of the equation governing enstrophy dynamics, enstrophy being the scalar counterpart to rotation, and enstrophy appears in the equation governing the strain-rate tensor's dynamics as

$$\frac{1}{2} \frac{D\omega^2}{Dt} = \omega_i S_{ij} \omega_j + \nu \omega_i \nabla^2 \omega_i, \quad (1.1)$$

$$\frac{1}{2} \frac{D(S_{ij} S_{ij})}{Dt} = -S_{ij} S_{jk} S_{ki} - \frac{1}{4} \omega_i S_{ij} \omega_j - S_{ij} \frac{\partial^2 p}{\partial x_i \partial x_j} + \nu S_{ij} \nabla^2 S_{ij}. \quad (1.2)$$

Turbulence, by its very nature, is multi-scaled with a general view that large eddies break up into smaller eddies, transferring turbulent kinetic energy along the energy cascade until viscous effects dominate and this energy is dissipated at the smallest scales (Richardson 1926; Batchelor & Townsend 1949; Kolmogorov 1962). In order to study the phenomenology of fine-scale turbulence, it is imperative to have a spatial resolution that is sufficiently high to resolve the flow down to these dissipative scales. Much of the earlier work pertaining to small-scale turbulent motions compared statistical estimates, such as probability density functions (p.d.f.s), skewness and flatness of gradient quantities such as enstrophy and dissipation (the scalar counterparts to rotation and strain, respectively). A review of such work can be found in the work of Sreenivasan & Antonia (1997). Statistical analysis of the small scales will not, however, reveal the instantaneous geometrical structure of the enstrophy and dissipation fields. In order to reveal this instantaneous topology, three-dimensional velocity and velocity gradient information is required. This three-dimensional information has become available through direct numerical simulation (DNS) studies (Siggia 1981; Kerr 1985; She, Jackson & Orszang 1990; Vincent & Meneguzzi 1991; Jiménez *et al.* 1993; Vincent & Meneguzzi 1994; da Silva & Pereira 2008). Hot wire probes (Kholmyansky, Tsinober & Yorish 2001), holographic particle image velocimetry (PIV) (Zhang, Tao & Katz 1997; Tao, Katz & Meneveau 2002) and cinematographic stereoscopic PIV (Matsuda & Sakakibara 2005; Ganapathisubramani, Lakshminarasimhan & Clemens 2007, 2008) have also been employed, recently, to gather this three-dimensional velocity and velocity gradient data experimentally.

The topological evolution of a fluid element is characterized by the eigenvalues (s_i) of the rate of strain tensor (S_{ij}) (Betchov 1956). The eigenvalues s_1 and s_3 correspond to the extensive and compressive strain rates, respectively, i.e. $s_1 > 0$, $s_3 < 0$, whereas s_2 , the intermediate eigenvalue, can be either extensive or compressive, bounded by the values of s_1 and s_3 such that $s_1 > s_2 > s_3$. Continuity ($\nabla \cdot \mathbf{u} = 0$) demands $s_1 + s_2 + s_3 = 0$. The fact that the intermediate strain rate can be either extensive (positive) or compressive (negative) suggests that it will determine the nature of the topological evolution of a particular fluid element. Elements for which there are two orthogonal extensive strain rates ($s_1, s_2 > 0$) acting in conjunction with the orthogonal compressive strain rate tend to form 'sheet-like' structures. By contrast, elements for which there are two orthogonal compressive strain rates ($s_2, s_3 < 0$) acting in conjunction with the orthogonal extensive strain rate tend to form 'tube-like' topology.

A large proportion of the work with good spatial resolution, investigating the small scales of turbulence, has focused on the structure and geometry of regions of high enstrophy. By isolating regions of intense enstrophy, using various vortex identification methods as described by Jeong & Hussain (1995) and Chakraborty, Balachandar & Adrian (2005), several studies have shown strongly swirling structures to be ‘tube/worm-like’ (Kerr 1985; Ashurst *et al.* 1987; Vincent & Meneguzzi 1991; Jiménez *et al.* 1993). These ‘worms’ have been shown to have characteristic diameters on the order of 10η , where η is the Kolmogorov length scale, and have been shown to extend up to 40η in length (Ganapathisubramani *et al.* 2008). These ‘worms’ had been thought to be embedded in a ‘random sea’ of structureless weak vorticity, which has been considered to be nearly Gaussian (Jiménez *et al.* 1993). Ruetsch & Maxey (1991) showed that within this ‘random sea’ there exist regions of intensely dissipating fluid that tend to surround the high enstrophy ‘worms’ and are topologically ‘sheet-like’. A clearer picture of the ‘random sea’ is now emerging suggesting that it is not entirely random and is organized into distinct structures of its own (Tsinober, Shtilman & Vaisburd 1997). Regions of weaker enstrophy have also been found to be far more dynamically important in turbulence than was previously thought, especially with regard to nonlinear processes such as strain and enstrophy production (Tsinober 1998; Tsinober, Ortenberg & Shtilman 1999).

It can be seen that (1.1), describing enstrophy dynamics, consists of a vortex stretching term ($\omega_i S_{ij} \omega_j$) and a viscous dissipation term. The $\omega_i S_{ij} \omega_j$ term describes the effects of local amplification of enstrophy by vortex filament stretching (an inviscid mechanism) and the $\nu \omega_i \nabla^2 \omega_i$ term represents the spread of vorticity due to viscosity (Morton 1984). Moreover, the enstrophy amplification term is the scalar product of the vorticity vector with the vortex stretching vector ($\mathbf{W} = S_{ij} \omega_j$). Taylor (1938) first showed that $\langle \omega_i S_{ij} \omega_j \rangle > 0$, that is to say, on average, enstrophy production (vortex stretching) prevails over enstrophy destruction (vortex compression). This has subsequently been shown both numerically (Betchov 1975) and experimentally (Tsinober, Kit & Dracos 1992). The magnitude of the enstrophy production term, which can be used as a measure of nonlinearity (Tsinober *et al.* 1999), is (Betchov 1956)

$$\omega_i S_{ij} \omega_j = \omega^2 s_i (\hat{\mathbf{e}}_i \cdot \hat{\boldsymbol{\omega}})^2, \quad (1.3)$$

where $\hat{\mathbf{e}}_i$ and $\hat{\boldsymbol{\omega}}$ are the normalized strain-rate eigenvectors (corresponding to s_i) and vorticity vector, respectively. The importance of the interaction between rotation and straining is exemplified by the fact that (nonlinear) enstrophy production is determined by the cosines of the alignment angle between the vorticity vector and the principal axes of the rate of strain tensor.

The preponderance of the vorticity vector to be aligned with the intermediate strain-rate eigenvector was first observed by Ashurst *et al.* (1987) and subsequently confirmed by several other studies (e.g. Tsinober *et al.* 1992; Tanahashi, Iwase & Miyauchi 2001; Mullin & Dahm 2006). Jiménez (1992) offers an explanation for this by using a two-dimensional argument. Andreotti (1997) showed that the tendency for the vorticity vector to align with the intermediate strain-rate eigenvector is a result of the crossover of the eigenvalues. This led to the development of an alternative reordering of the eigenvalues in which the eigenvalue with the corresponding eigenvector that is most closely aligned with the vorticity vector is denoted σ_z , with the largest of the two remaining eigenvalues denoted σ_+ and the smallest one denoted as σ_- (Andreotti 1997; Nomura & Post 1998; Horiuti 2001). However, in the current study, the eigenvalues would have more physical meaning when arranged by magnitude as it would be

clear that the corresponding eigenvector would be compressive, extensive or alternate. This information is far more difficult to present when the eigenvalues are reordered according to the preferential alignment with the vorticity vector. Although most regions show a preference for the vorticity vector to align with the intermediate strain-rate eigenvector, Tsinober *et al.* (1997) and Kholmyansky *et al.* (2001) observed that regions in which the vorticity vector is aligned to the extensive strain-rate eigenvector make the largest contribution to the enstrophy production. Hamlington *et al.* (2008) examined the alignment between the vorticity vector and the strain-rate eigenvectors and stated that whilst the vorticity vector is preferentially aligned to the intermediate eigenvector of the local strain rate, it tends to align with the extensive eigenvector of the non-local strain rate. However, the overall p.d.f. for the alignment between the vorticity vector and the extensive strain-rate eigenvector is flat, indicating an arbitrary alignment between the two vectors (e.g. Ashurst *et al.* 1987).

More recently, Buxton & Ganapathisubramani (2009) examined the alignment between the eigenvectors of the rate of strain tensor (\mathbf{e}_i) and the ‘swirling eigenvector’ (\mathbf{v}_r). The ‘swirling eigenvector’ is defined as the real eigenvector of the velocity gradient tensor ($D_{ij} = \partial u_i / \partial x_j$), when D_{ij} has a real and complex conjugate pair of eigenvalues and corresponding eigenvectors. When this is the case, the local streamlines are spiralling/swirling in nature with the magnitude of the imaginary part of the complex conjugate pair of eigenvalues (λ_{ci}) characterizing the local swirling strength and the real eigenvector defining the axis of swirling (Zhou *et al.* 1999). The study observed that whilst the vorticity vector did indeed preferentially align with the intermediate strain-rate eigenvector (\mathbf{e}_2), \mathbf{v}_r instead tended to align with \mathbf{e}_1 , the extensive strain-rate eigenvector.

This study aims to investigate the nonlinear enstrophy production term ($\omega_i S_{ij} \omega_j$) in the turbulent far field of an axisymmetric turbulent jet. Cinematographic stereoscopic PIV data is used as the basis for this investigation. Particular emphasis is given to comparing enstrophy production in swirling ($\lambda_{ci} > 0$) and straining ($\lambda_{ci} = 0$) regions, by means of examining the alignment of the eigenvectors of the rate of strain tensor (\mathbf{e}_i) with the vorticity vector ($\boldsymbol{\omega}$).

2. Experimental facility and techniques

The data used in this study was obtained by Ganapathisubramani *et al.* (2007) at the University of Texas, Austin, USA. The axisymmetric jet exhausted into a mild co-flow of air from a pipe of circular cross-section (diameter $D = 26$ mm), located at the centre of the co-flow facility. Tsurikov (2003), who developed the experimental facility, acquired velocity profiles using hot-film probes and documented the presence of a fully developed pipe flow at the jet axis. The spectra at the centreline indicated a $-5/3$ spectrum and had no dominant frequency. The jet velocity was $U_0 = 3$ m s⁻¹ and the co-flow velocity was $U_\infty = 0.15$ m s⁻¹. The boundary layer on the outside of the jet, due to the co-flow, was laminar with an estimated thickness of 11 mm near the jet exit. Additional details regarding design and construction of the flow facility and qualification of the flow field at the jet exit (i.e. axisymmetry of the jet, mean velocity profiles, turbulence intensities, etc.) are presented by Tsurikov (2003). Cinematographic stereoscopic PIV measurements were performed in the ‘end view’ plane (x_2 – x_3) at a downstream axial location of $x_1 = 32D$ (Note that in this study, x_1 is the axial direction and x_2 and x_3 are the two orthogonal radial directions). The seed particles were illuminated by a laser sheet of thickness ≈ 1 mm and the scattered light was captured by two CMOS cameras in stereoscopic arrangement oriented at an angle

of 30° to the axis of the jet. Cinematographic images were captured for a duration of 1 s, corresponding to a total of 2000 frames and 2 GB of data for each experimental run. The vector fields were computed by correlating successive particle images in the movie sequence ($\Delta t = 500 \mu\text{s}$, since the frequency of image acquisition was 2 kHz). The resulting vectors from each camera were then combined to compute all three velocity components. The final interrogation region was 16×16 pixels with 50 % overlap. A maximum pixel displacement with a magnitude of approximately seven pixels was observed for each camera. The resolution of the resulting stereoscopic vector fields is approximately $3\eta \times 3\eta$ ($1.35 \times 1.35 \text{ mm}^2$) and successive vectors are separated by 1.5η (due to 50 % overlap). The total field size is $160\eta \times 160\eta$ ($76 \times 76 \text{ mm}^2$). Due to intrinsic uncertainties associated with performing stereoscopic PIV measurements, the velocity field was not divergence free (i.e. $\nabla \cdot \mathbf{u} \neq 0$). The divergence error is in line with other experimental studies and is characterized and discussed further by Ganapathisubramani *et al.* (2007).

The relevant length scales at the measurement location are: jet half-width ($\delta_{1/2}$) = 126 mm, Taylor microscale (λ) = 13.8 mm and Kolmogorov scale (η) = 0.45 mm. The Kolmogorov scale is defined as $\eta = (\nu^3 / \langle \epsilon \rangle)^{1/4}$, where ν is the kinematic viscosity and $\langle \epsilon \rangle$ is the mean rate of dissipation which was calculated from the experimental data. The Reynolds number based on jet exit velocity and diameter is $Re_D = 5100$ and the Reynolds number based on Taylor microscale is $Re_\lambda \approx 150$.

Taylor's hypothesis, with a convection velocity equal to the local mean axial velocity $\bar{u}_1(x_2, x_3)$ (u_1, u_2 and u_3 are the velocity components along the x_1, x_2 and x_3 directions respectively), was utilized to reconstruct a quasi-instantaneous space-time volume of this filtered data in order to produce three-dimensional flow visualizations. The convection velocity (i.e. the mean axial velocity) varies over the x_2 - x_3 plane and consequently the axial coordinates are different for different regions of the jet. Additional information regarding the experimental setup and validation are given by Ganapathisubramani *et al.* (2007, 2008).

3. Statistical results

A p.d.f. for the enstrophy production rate, $\omega_i S_{ij} \omega_j$, is presented in figure 1. This data, and all subsequent data, are non-dimensionalized by the suitable combination of ν and η , where ν is the kinematic viscosity and η is the Kolmogorov length scale. The general consensus in the literature (Taylor 1938; Tennekes & Lumley 1972 amongst others) is that vortex stretching ($\omega_i S_{ij} \omega_j > 0$) is favoured over vortex compression ($\omega_i S_{ij} \omega_j < 0$) in high-Reynolds-number flows. This is borne out in the figure, which shows that there is a significant peak just above zero. Additionally, the positive tail of the p.d.f. is 'fatter' than the negative one indicating further that enstrophy production is favoured over enstrophy destruction in turbulent flows resulting in a positive mean value of $\langle \omega_i S_{ij} \omega_j \rangle = 0.07(\nu/\eta^2)^3$. The shape of this p.d.f. agrees well with the dual plane stereo PIV study of Mullin & Dahm (2006).

Equation (1.3) illustrates the importance to the overall enstrophy production rate of the alignment of the vorticity vector to the strain-rate tensor eigenvectors. Figure 2 shows p.d.f.s for the cosines of the alignment angle between the rate of strain tensor eigenvectors and the vorticity vector. In order to distinguish between swirling and straining regions, the discriminant of the characteristic equation for the eigenvalues of the velocity gradient tensor (see (3.1)), D , is employed. When D is positive, the eigenvalues are complex and the streamlines are locally swirling (Zhou *et al.* 1999) and the quantity $\lambda_{ci} = \sqrt{D}$ is used as a measure of the local swirling strength. When

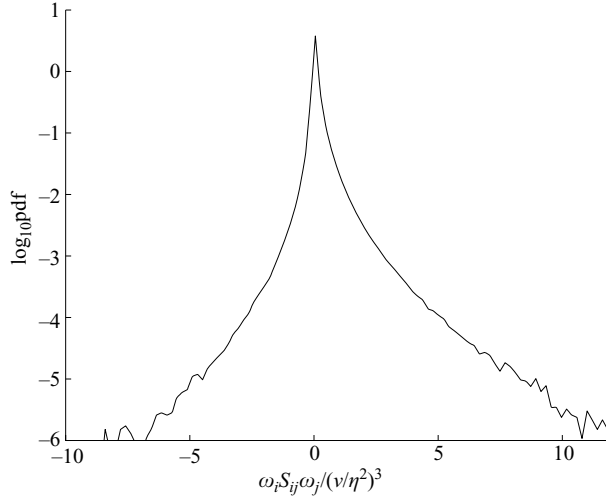


FIGURE 1. Probability density function (p.d.f.) for the enstrophy production rate $(\omega_i S_{ij} \omega_j)$ normalized by $(\nu/\eta^2)^3$, where ν is the kinematic viscosity and η is the Kolmogorov length scale. Note that the ordinate axis is logarithmic.

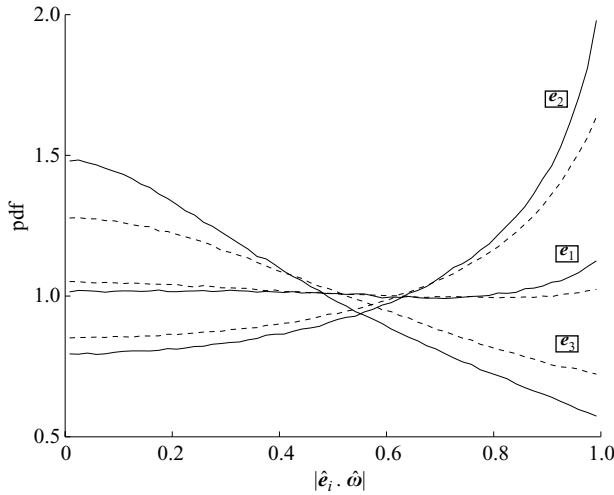


FIGURE 2. Probability density functions (p.d.f.s) of cosine of the alignment angle between the eigenvectors of the rate of strain tensor (e_i) and the vorticity vector (ω). The solid lines are p.d.f.s constructed from regions for which $\lambda_{ci} = 0$, i.e. there is no local swirling and the dashed lines are for $\lambda_{ci} > 0$, i.e. local swirling is present.

D is negative (real eigenvalues only), there is no local swirling present (straining only) and λ_{ci} is set to zero. In the data presented here, regions with a non-zero value of λ_{ci} , hence swirling regions, accounted for 62% of the volume investigated. Over all these regions, for which there was a local swirl defined, the mean value $\langle \lambda_{ci} \rangle = 21.1 \text{ s}^{-1}$. The solid lines of figure 2 are p.d.f.s constructed from all regions for which there is no local swirling defined ($\lambda_{ci} = 0$) and the dashed lines are constructed from regions for which there is a local swirl defined ($\lambda_{ci} > 0$). The tendency for ω to preferentially align

with the intermediate strain-rate eigenvector (\mathbf{e}_2) can be observed from the peak in both the straining and swirling p.d.f.s at $|\hat{\mathbf{e}}_2 \cdot \hat{\boldsymbol{\omega}}| = 1$, in agreement with the literature. Additionally, the tendency for $\boldsymbol{\omega}$ to be perpendicular to the compressive strain-rate eigenvector (peaks at $|\hat{\mathbf{e}}_3 \cdot \hat{\boldsymbol{\omega}}| = 0$) and arbitrarily aligned with the extensive strain-rate eigenvector (flat p.d.f.s for $|\hat{\mathbf{e}}_1 \cdot \hat{\boldsymbol{\omega}}|$) can be observed in figure 2. The tendency for $\boldsymbol{\omega}$ to align with \mathbf{e}_2 and to be perpendicular to \mathbf{e}_3 is exaggerated (higher peak in solid line p.d.f. values) for straining regions as opposed to swirling regions. A slight peak in the solid line p.d.f. suggests that there is a slight preference for $\boldsymbol{\omega}$ to align with \mathbf{e}_1 in straining regions.

The effects of vorticity–strain-rate eigenvector alignment upon enstrophy production rate can be further examined by categorizing the regions using the second and third invariants of the characteristic equation for the eigenvalues of D_{ij} , the velocity gradient tensor. This characteristic equation is given by

$$\lambda^3 + P\lambda^2 + Q\lambda + R = 0. \quad (3.1)$$

The second invariant, Q , can be written as $(1/2)(\|\Omega_{ij}\|^2 - \|S_{ij}\|^2)$ for an incompressible flow and can be used as a vortex identification criterion as it illustrates the local excess of rotation over strain rate (Chakraborty *et al.* 2005). P and R are the first and third invariants and are defined as $\nabla \cdot \mathbf{u}$ ($= 0$ for an incompressible flow) and $-\det(D_{ij})$, respectively. The study of Chong, Perry & Cantwell (1990) used a Q – R plane as a means of characterizing different flow behaviour. Figure 3 shows a joint p.d.f. between Q and R . Dashed lines mark $R = 0$ and $D = 0$ (where D is the discriminant of the characteristic equation (3.1)) in order to split the data into four sectors. The Q – R plane has been shown to unambiguously determine the local topology of the fluid motion (Martín *et al.* 1998). In P – Q – R space, the equation for the surface that separates purely real from complex roots is (Chong *et al.* 1990)

$$27R^2 + (4P^3 - 18PQ)R + (4Q^3 - P^2Q^2) = 0. \quad (3.2)$$

In a completely divergence-free flow ($\nabla \cdot \mathbf{u} = 0$ i.e. $P = 0$), the equation for D is given by $D = Q^3 + (27/4)R^2$. Regions for $D > 0$ are thus swirling, whereas points for which $D < 0$ are straining only (Perry & Chong 1994). Due to the limitations of the experimental techniques used to gather the data, the velocity field is not completely divergence free (hence $P \neq 0$). This leads to some purely real solutions (straining only) for $D > 0$ and complex solutions (swirling) for $D < 0$ (see Ganapathisubramani *et al.* (2008) for more details on limitations of the experimental technique). The four sectors are defined as $D > 0; R > 0$ (S1 for brevity), $D < 0; R > 0$ (S2), $D < 0; R < 0$ (S3) and $D > 0; R < 0$ (S4). The p.d.f.s for the alignment tendencies of the extensive (\mathbf{e}_1) and intermediate (\mathbf{e}_2) strain-rate eigenvectors with $\boldsymbol{\omega}$ in the four sectors are presented beneath the Q – R plot.

The largest of the sectors is S4, accounting for 37 % of the total volume. This sector is dominated by swirling with 96 % of the volume within S4 exhibiting local swirling, for which the mean value is $\langle \lambda_{ci} \rangle_{S4} = 1.16 \langle \lambda_{ci} \rangle$. The sector S4 is also responsible for a large proportion of the total enstrophy production rate $\langle \omega_i S_{ij} \omega_j \rangle_{S4} = 2.44 \langle \omega_i S_{ij} \omega_j \rangle$, with 93 % of the constituent volume having a positive value of $\omega_i S_{ij} \omega_j$. The alignment p.d.f. for S4 shows that there is a large peak at $|\hat{\mathbf{e}}_1 \cdot \hat{\boldsymbol{\omega}}| = 1$ (the solid line p.d.f.) indicating that the vorticity vector aligns with the extensive strain-rate eigenvector in S4. This strong alignment with the extensive strain-rate eigenvector (relative to S1 and S2) encourages vortex stretching and hence enstrophy production.

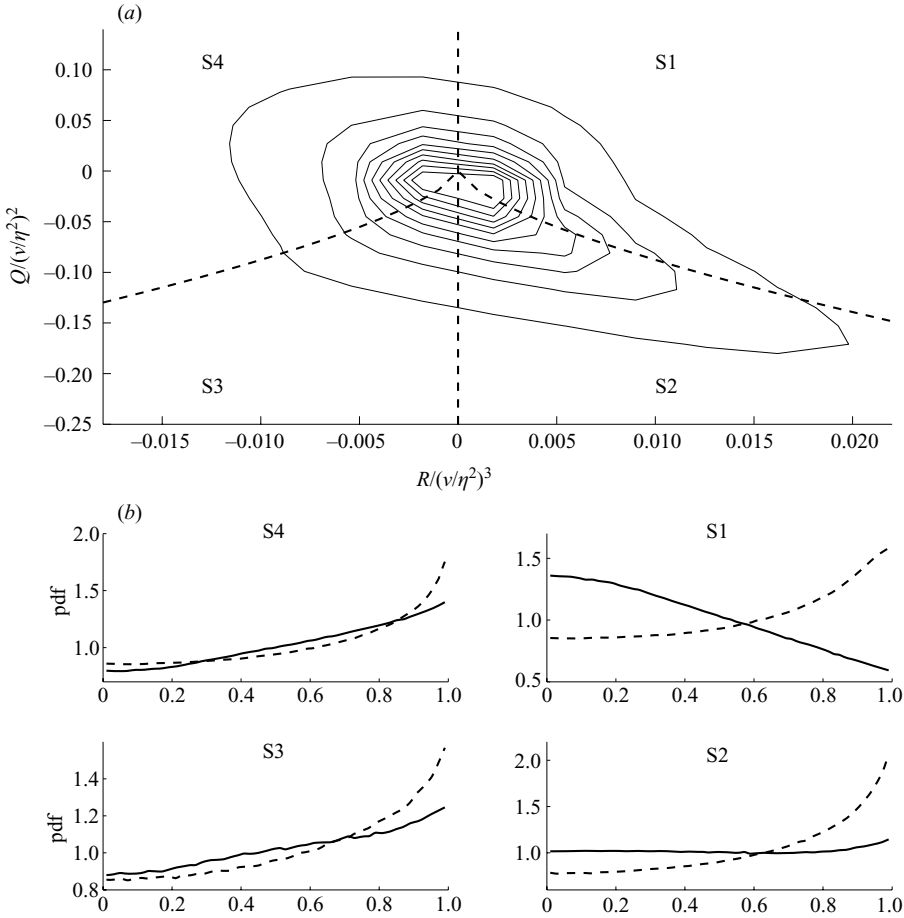


FIGURE 3. Joint p.d.f. between Q and R , the second and third invariants of the characteristic equation for the eigenvalues of the velocity gradient tensor, normalized by the second and third powers of v/η^2 , respectively. The outer contour is at level 70 and the inner contour is at level 700. The spacing between adjacent contour levels is 70. The dashed lines mark $R=0$ and $D=Q^3+(27/4)R^2=0$ (D is the discriminant of the characteristic equation). Below the Q - R plot are p.d.f.s illustrating the alignment tendencies ($|\hat{e}_i \cdot \hat{\omega}|$) of ω with e_1 (solid lines) and e_2 (dashed lines) in the four sectors marked on the joint p.d.f.

The p.d.f. for sector S3 also shows a peak at $|\hat{e}_1 \cdot \hat{\omega}|=1$, illustrating a tendency for the vorticity vector to align with the extensive strain-rate eigenvector. This sector shows a moderate positive enstrophy production rate ($\langle \omega_i S_{ij} \omega_j \rangle_{S3} = 0.54 \langle \omega_i S_{ij} \omega_j \rangle$); this is smaller than $\langle \omega_i S_{ij} \omega_j \rangle$ due to the fact that 35% of points within S3 possess negative values of $\omega_i S_{ij} \omega_j$. S3 is a sector that is dominated by straining regions, with 93% of the regions exhibiting no local swirling. This sector is comprised of only 10% of the total volume.

Note that S2 is another sector that is dominated by straining regions ($D < 0$) with 92% of the constituent points exhibiting no local swirling. The mean enstrophy production rate is also moderate, $\langle \omega_i S_{ij} \omega_j \rangle_{S2} = 0.69 \langle \omega_i S_{ij} \omega_j \rangle$, with a slightly greater proportion of points (80%) displaying positive $\omega_i S_{ij} \omega_j$ than S3. This sector accounts for 24% of the overall volume.

Sector (S)	Proportion of total volume (%)	$\langle \omega_i S_{ij} \omega_j \rangle_S / \langle \omega_i S_{ij} \omega_j \rangle$	$\langle \lambda_{ci} \rangle_S / \langle \lambda_{ci} \rangle$
S1	29	-0.40	0.47
S2	24	0.69	N/A
S3	10	0.54	N/A
S4	37	2.44	1.16

TABLE 1. Summary of mean enstrophy production rates ($\langle \omega_i S_{ij} \omega_j \rangle_S$) and mean swirling strength ($\langle \lambda_{ci} \rangle_S$) for the four sectors of the Q - R plane of figure 3.

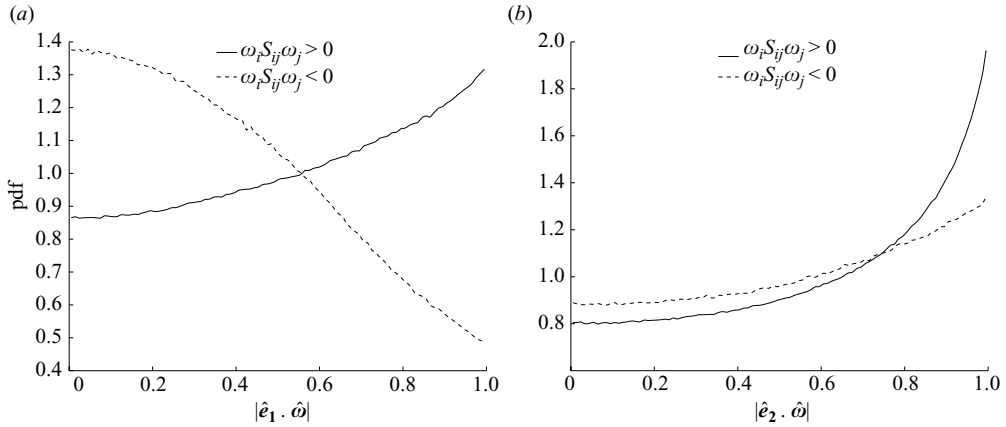


FIGURE 4. (a) Probability density function (p.d.f.) of cosine of alignment angle between the extensive strain-rate eigenvector (e_1) and the vorticity vector (ω) for enstrophy producing ($\omega_i S_{ij} \omega_j > 0$) and enstrophy destroying ($\omega_i S_{ij} \omega_j < 0$) regions. (b) Probability density function (p.d.f.) of cosine of alignment angle between the intermediate strain-rate eigenvector (e_2) and ω for enstrophy producing and enstrophy destroying regions.

Note that S1 is a weakly swirling region with 83% of the constituent volume exhibiting local swirling. The mean swirling strength is $\langle \lambda_{ci} \rangle_{S1} = 0.47 \langle \lambda_{ci} \rangle$. It is the only sector for which the mean rate of enstrophy production is negative (enstrophy destruction), with $\langle \omega_i S_{ij} \omega_j \rangle_{S1} = -0.40 \langle \omega_i S_{ij} \omega_j \rangle$, with 61% of the constituent points having $\omega_i S_{ij} \omega_j < 0$. The alignment p.d.f. for S1 shows a strong peak at $|\hat{e}_1 \cdot \hat{\omega}| = 0$ indicating that the vorticity vector tends to be perpendicular to the extensive strain-rate eigenvector, in stark contrast to the vortex stretching sectors S3 and S4. Also note that S1 is the second largest sector by constituent volume, accounting for 29% of the total number. The salient properties of all four sectors are summarized in table 1.

Several general observations can be made from figure 3. It can be seen that the e_2 - ω alignment p.d.f.s are qualitatively and quantitatively similar for all four sectors. By contrast, the e_1 - ω alignment p.d.f.s can be seen to vary significantly both qualitatively and quantitatively. The p.d.f.s of S3 and S4 are completely different in shape to that of S1 (a peak for the two vectors being perpendicular) and S2 (a flat p.d.f. indicating arbitrary alignment). It can thus be concluded that the alignment between the vorticity vector and the extensive strain-rate eigenvector is crucial in determining whether the amplification of enstrophy is positive (parallel) or negative (perpendicular). The role of the alignment between the intermediate strain-rate eigenvector and the vorticity vector is of much less significance. This can be seen in figure 4 that shows that e_1 - ω

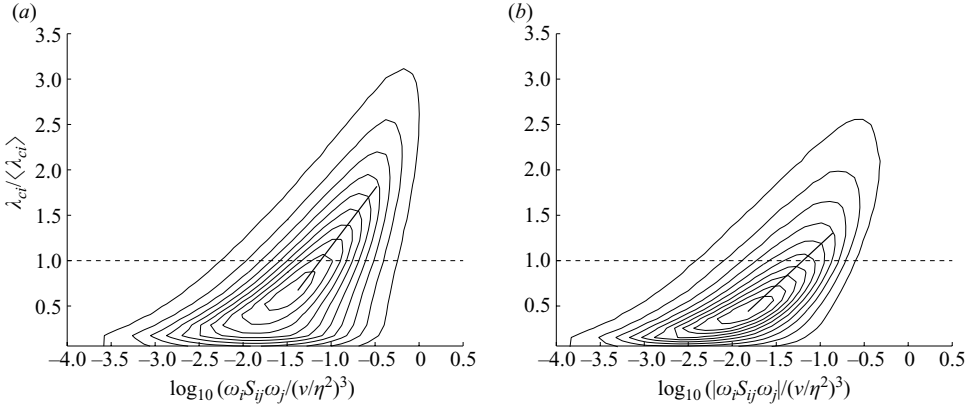


FIGURE 5. (a) Joint p.d.f. between local swirling strength (λ_{ci}) and the logarithm of the normalized enstrophy production rate ($\omega_i S_{ij} \omega_j$) for regions in which this term is positive (enstrophy production). The outer contour level is 0.045 and the inner contour level is 0.45. The separation between successive contour levels is 0.045. (b) Joint p.d.f. between λ_{ci} and the logarithm of the magnitude of $\omega_i S_{ij} \omega_j$ for regions in which this term is negative (enstrophy destruction). The outer contour is at level 0.06 and the inner contour is at level 0.6. The separation between successive contour levels is 0.06. The dashed lines in both figures illustrate the mean value of local swirling strength, $\langle \lambda_{ci} \rangle = 21.1 \text{ s}^{-1}$.

alignment p.d.f.s are completely different for $\omega_i S_{ij} \omega_j > 0$ and $\omega_i S_{ij} \omega_j < 0$. The p.d.f. for vortex stretching points (i.e. $\omega_i S_{ij} \omega_j > 0$) shows a clear peak for parallel alignment between \mathbf{e}_1 and $\boldsymbol{\omega}$, whereas the vortex compression p.d.f. shows a peak when the two vectors are perpendicular. The ‘traditionally’ flat p.d.f. for \mathbf{e}_1 – $\boldsymbol{\omega}$ alignment (shown in figure 2) can thus be seen to be the summation of the distinctly different alignment behaviour of vortex stretching and vortex compression regions. By contrast, the p.d.f.s of \mathbf{e}_2 – $\boldsymbol{\omega}$ alignment shown in figure 4(b) are qualitatively similar for both vortex stretching and vortex compression regions, albeit with a more arbitrary alignment (lower peak value) for the $\omega_i S_{ij} \omega_j < 0$ case.

Although sectors S2, S3 and S4 favour enstrophy production over destruction, S4 has a much larger mean enstrophy production rate than the other two sectors. Of these three sectors, S4 predominantly contains swirling regions, whereas S2 and S3 are dominated by straining regions. Figure 5(a) shows a joint p.d.f. between the logarithm of $\omega_i S_{ij} \omega_j$ and the local swirling strength (λ_{ci}) constructed from regions for which $\omega_i S_{ij} \omega_j > 0$, i.e. enstrophy producing regions. The dashed line on the figure illustrates the mean local swirling rate, $\langle \lambda_{ci} \rangle$. Of the enstrophy producing regions ($\omega_i S_{ij} \omega_j > 0$), 36 % are weakly swirling ($0 < \lambda_{ci} < \langle \lambda_{ci} \rangle$) and 40 % are straining ($\lambda_{ci} = 0$). However, the weakly swirling and straining regions account for only 18 % and 21 % of the total enstrophy production (positive $\omega_i S_{ij} \omega_j$), respectively. Strongly swirling regions ($\lambda_{ci} > \langle \lambda_{ci} \rangle$), whilst accounting for only 24 % of the volume, contribute 61 % of the total enstrophy production rate. This is further supported by the fact that the joint p.d.f. contours slope towards higher $\omega_i S_{ij} \omega_j$ for higher λ_{ci} , suggesting that higher enstrophy production rates are associated with higher local swirling. This clearly mirrors the finding that S4, the most strongly swirling sector in the Q – R plane, is also the sector with the highest enstrophy production rate.

Figure 5(b) shows the joint p.d.f. between the logarithm of the magnitude of $\omega_i S_{ij} \omega_j$ and λ_{ci} constructed from regions for which $\omega_i S_{ij} \omega_j < 0$, i.e. enstrophy destroying regions. It can be seen that the inner most contours do not slope as steeply towards

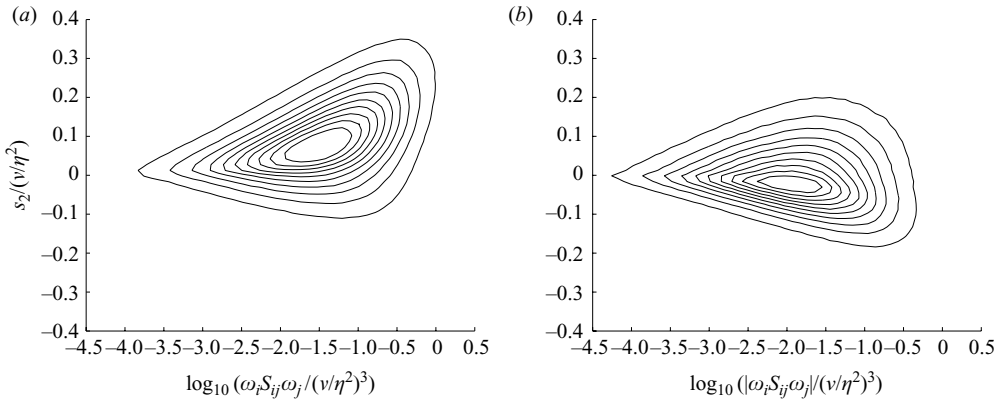


FIGURE 6. (a) Joint p.d.f. between the intermediate strain rate (s_2) and the logarithm of the enstrophy production rate ($\omega_i S_{ij} \omega_j$) for regions in which this term was positive (enstrophy production). The outer contour is at level 0.22 and the inner contour is at level 2.2. The separation between successive contour levels is 0.22. (b) Joint p.d.f. between s_2 and the logarithm of the magnitude of $\omega_i S_{ij} \omega_j$ for regions in which this term was negative (enstrophy destruction). The outer contour is at level 0.25 and the inner contour is at level 2.5. The separation between successive contour levels is 0.25.

high λ_{ci} with increasing enstrophy destruction rate as the contours of the joint p.d.f. in figure 5(a) do for increasing enstrophy production rate. This is illustrated by the steeper tangent to the joint p.d.f. in figure 5(a) than that of figure 5(b). In addition, the contours do not extend as far into high values of λ_{ci} as those of the enstrophy production joint p.d.f. in figure 5(a). This figure thus mirrors the finding that enstrophy destruction ($\omega_i S_{ij} \omega_j < 0$) is predominantly observed in weakly swirling regions, such as those found in S1.

Figure 6(a) shows the joint p.d.f. between the intermediate strain rate (s_2) and the logarithm of the enstrophy production rate ($\omega_i S_{ij} \omega_j$) for regions in which this term was positive (i.e. enstrophy production). Due to the fact that s_2 can be either extensive or compressive, it determines whether a fluid element will tend to form ‘sheet-like’ ($s_2 > 0$) or ‘tube-like’ topology ($s_2 < 0$). It can be seen that the contours of the joint p.d.f. in figure 6(a) extend further in the positive s_2 domain than the negative s_2 domain, and that they slope towards positive s_2 for more strong vortex stretching regions, suggesting that intensely vortex stretching regions coincide with positive s_2 . It can therefore be concluded that enstrophy producing regions tend to be ‘sheet-forming’ (as shown by Betchov 1956), particularly so for strong enstrophy producing (vortex stretching) regions.

Figure 6(b) shows the joint p.d.f. between s_2 and the logarithm of the magnitude of $\omega_i S_{ij} \omega_j$ for regions in which this term was negative (i.e. enstrophy destruction). The contours of the p.d.f. extend approximately the same distance in the positive and negative s_2 domains, in contrast to those of figure 6(a). Additionally, the degree to which the contours in figure 6(b) extend in either direction is significantly smaller than that in figure 6(a). This suggests that enstrophy destroying regions on the whole tend to be a combination of weakly ‘sheet-forming’ and weakly ‘tube-forming’ topologies. It can thus be concluded that enstrophy producing regions have a more distinct tendency to form uniform (‘sheet-like’) topologies, due to the strong skew to positive s_2 of the joint p.d.f. of figure 6(a), than enstrophy destroying regions which do not have a clear ‘sheet-forming’ or ‘tube-forming’ tendency.

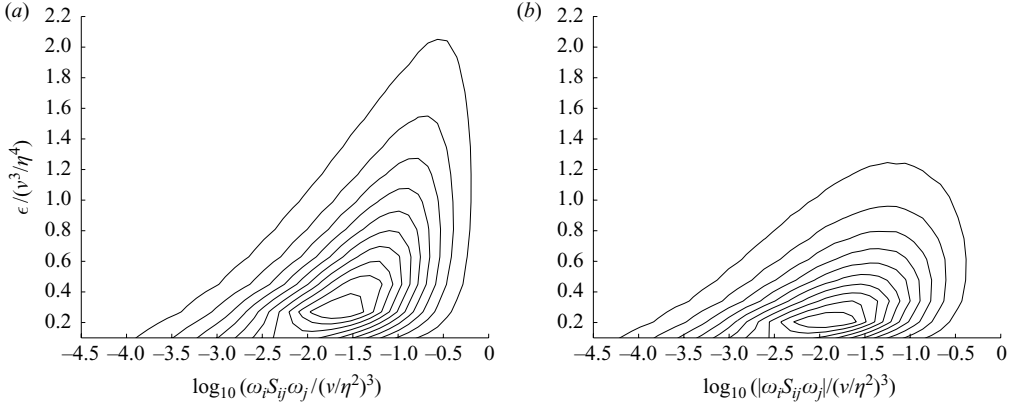


FIGURE 7. (a) Joint p.d.f. between the normalized dissipation rate (ϵ) and the logarithm of the enstrophy production rate ($\omega_i S_{ij} \omega_j$) for regions in which this term was positive (enstrophy production). The outer contour is at level 0.065 and the inner contour is at level 0.65. The separation between successive contour levels is 0.065. (b) Joint p.d.f. between ϵ and the logarithm of the magnitude of $\omega_i S_{ij} \omega_j$ for regions in which this term was negative (enstrophy destruction). The outer contour is at level 0.085 and the inner contour is at level 0.85. The separation between successive contour levels is 0.085.

Figures 5 and 6 show that strong enstrophy producing regions tend to be ‘sheet-forming’ and swirling. Previous studies have shown that regions of intense kinetic energy dissipation rate are observed as ‘sheet-like’ structures that surround the high enstrophy ‘worms’ (for example see Ganapathisubramani *et al.* 2008). Therefore the relationship between enstrophy producing and enstrophy destroying regions with respect to the kinetic energy dissipation rate is explored. Figure 7(a) shows the joint p.d.f. between the logarithm of $\omega_i S_{ij} \omega_j$ and the kinetic energy dissipation rate (ϵ) for regions in which $\omega_i S_{ij} \omega_j > 0$. The kinetic energy dissipation rate is non-dimensionalized by the mean, $\langle \epsilon \rangle = v^3/\eta^4 = 0.085 \text{ m}^2 \text{ s}^{-3}$. The contours are observed to slope towards higher ϵ for higher $\omega_i S_{ij} \omega_j$. This is in contrast with the contours of the joint p.d.f. between ϵ and the logarithm of the magnitude of $\omega_i S_{ij} \omega_j$ of figure 7(b). It can be seen that the shape of the joint p.d.f. in figure 7(b) is more round with a significantly reduced tendency for the contours to slope towards higher ϵ for higher enstrophy destruction rates. The contours also extend to much higher ϵ for the enstrophy producing joint p.d.f. than for the enstrophy destroying joint p.d.f. It can thus be stated that there is a tendency for highly enstrophy producing regions to coincide with intensely kinetic energy dissipating regions as observed by Tsinober *et al.* (1997), Tsinober (1998) and Gulitski *et al.* (2007). This is not the case for enstrophy destroying regions, which tend to be found in regions for which the kinetic energy dissipation rate is only moderate.

Andreotti (1997) developed a method whereby vortex sheets, such as those that surround ‘worms’, can be deduced directly. Horiuti & Takagi (2005) stated that the most prominent characteristic feature of a vortex sheet is that the strain rate and the vorticity are highly correlated and their magnitudes comparably large. This correlation between strain rate and vorticity is one of the key reasons for positive enstrophy amplification to take place within these vortex sheets. The method uses an eigenvalue ($[A_{ij}]_+$) of the second-order velocity gradient tensor, $A_{ij} = (S_{ik} \Omega_{kj} + S_{jk} \Omega_{ki})$, which is a term contained in the decomposition of the Reynolds stress tensor using the nonlinear model (Horiuti 2003). It can be shown that $[A_{ij}]_+$ can be approximated

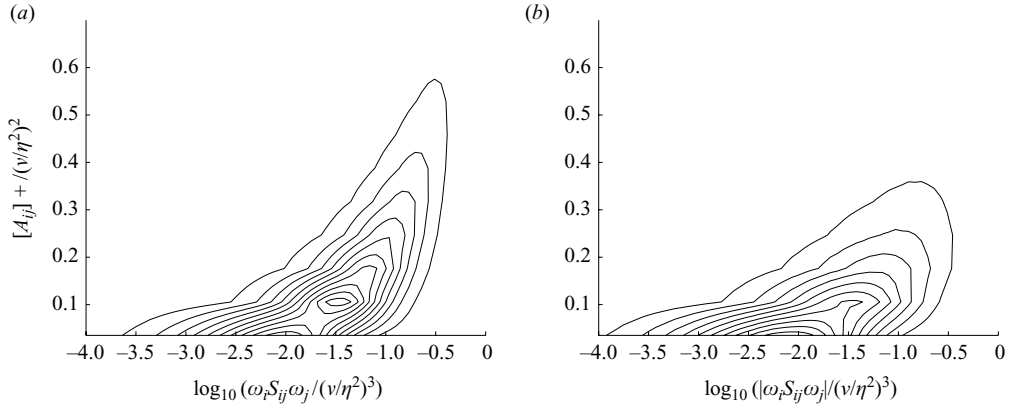


FIGURE 8. (a) Joint p.d.f. between $[A_{ij}]_+$ and the logarithm of the enstrophy production rate ($\omega_i S_{ij} \omega_j$) for regions in which this term was positive (enstrophy production). The outer contour is at level 0.3 and the inner contour is at level 3. The separation between successive contour levels is 0.3. (b) Joint p.d.f. between $[A_{ij}]_+$ and the logarithm of the magnitude of $\omega_i S_{ij} \omega_j$ for regions in which this term was negative (enstrophy destruction). The outer contour is at level 0.45 and the inner contour is at level 4.5. The separation between successive contour levels is 0.45.

as $[A_{ij}]_+ \simeq +\sqrt{(1/2)A_{ij}A_{ji}}$ in practice (Horiuti & Takagi 2005). Figure 8(a) shows the joint p.d.f. between the logarithm of $\omega_i S_{ij} \omega_j$ and $[A_{ij}]_+$ for regions in which $\omega_i S_{ij} \omega_j > 0$. Qualitatively, this joint p.d.f. is similar to that of figure 7(a) with the contours sloping towards higher $[A_{ij}]_+$ for higher $\omega_i S_{ij} \omega_j$. This reinforces the statistical observation that enstrophy production is focused in vortex sheets. The shape of this joint p.d.f. is again in contrast with that of figure 8(b), which shows the joint p.d.f. between $[A_{ij}]_+$ and the logarithm of the magnitude of $\omega_i S_{ij} \omega_j$ for regions of enstrophy destruction. Again, the contrast between these two figures is similar to that for figure 7 thereby reinforcing the finding that strong enstrophy producing regions tend to be found in more distinct vortex sheets than enstrophy destroying regions do.

Statistical results indicate the tendencies of the amplification of enstrophy to be ‘sheet-forming’ for vortex stretching regions but with no preference to form either ‘tube-like’ or ‘sheet-like’ topology for vortex compressing regions. High rates of enstrophy production (vortex stretching) are also observed to tend to coincide with strong swirling, as well as highly dissipative, regions of the flow. The three-dimensional nature of the stereoscopic PIV data allows a quasi-instantaneous volume of data to be created using Taylor’s hypothesis, thereby allowing the statistical findings to be compared to instantaneous visualizations of the flow. These comparisons are presented in the next section.

4. Instantaneous results

Figure 9(a) shows instantaneous isosurfaces of regions of strong vortex stretching ($\omega_i S_{ij} \omega_j = 4 \times 10^5 \text{ s}^{-3} = 0.96(\nu/\eta^2)^3$). Just under 2% of the total data exceed this $\omega_i S_{ij} \omega_j$ threshold, yet they account for 23% of the total enstrophy production rate ($\omega_i S_{ij} \omega_j > 0$). Taylor’s hypothesis is used to produce the volume displayed in figures 9(a) and (b) from 200 instantaneous PIV frames; see Ganapathisubramani *et al.* (2007, 2008) for further details on volume reconstruction. The figure shows that regions of intense vortex stretching appear to be, on the whole, topologically

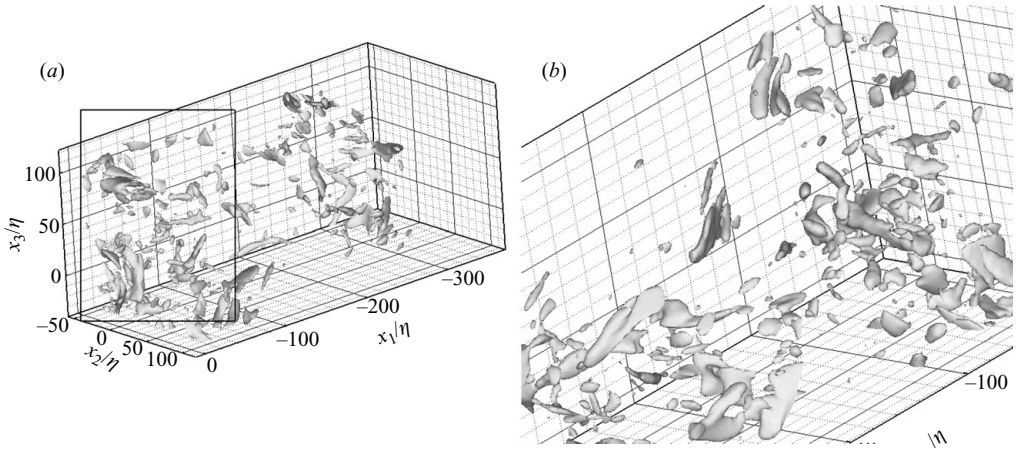


FIGURE 9. (a) Isosurfaces of enstrophy production rate, $\omega_i S_{ij} \omega_j = 4 \times 10^5 \text{ s}^{-3} = 0.96(v/\eta^2)^3$. (b) A close-up from a different perspective of the isosurfaces of $\omega_i S_{ij} \omega_j = 4 \times 10^5 \text{ s}^{-3}$ within the black rectangle shown in (a). Taylor's hypothesis was used to construct the volume from 200 instantaneous PIV frames. The axes are scaled by the Kolmogorov length scale, η .

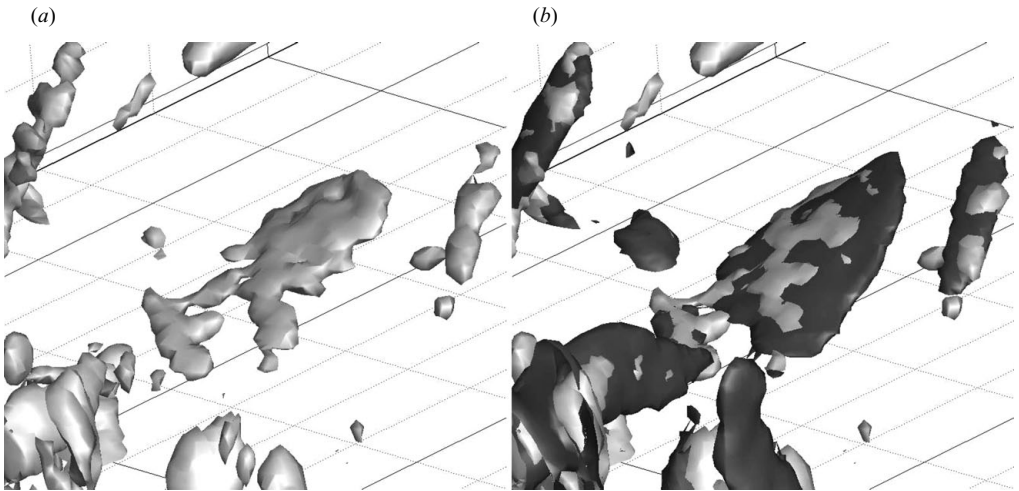


FIGURE 10. (a) An individual example of a sheet of $\omega_i S_{ij} \omega_j$. (b) The same sheet of enstrophy production rate from (a) shown with isosurfaces of $[A_{ij}]_+ = 1.43(v/\eta^2)^2$.

'sheet-like'. Visualizing these isosurfaces from other perspective directions, such as figure 9(b), reinforces this point. An example of a 'sheet-like' structure of enstrophy production rate is presented in figure 10(a). This instantaneous observation is also consistent with the statistical findings presented in figure 6(a). The joint p.d.f. in figure 6(a) shows that strong enstrophy producing regions are particularly likely to coincide with an extensive intermediate strain rate and thus tend to be topologically 'sheet-forming'. The figure also shows, however, that a smaller proportion of strong enstrophy production regions have a negative value of s_2 , hence topologically 'tube-forming' regions of enstrophy production also exist. It should be noted that whilst s_2 characterizes the topology forming tendencies of a fluid element, it does not necessarily describe the instantaneous topology of a turbulent structure. However, if

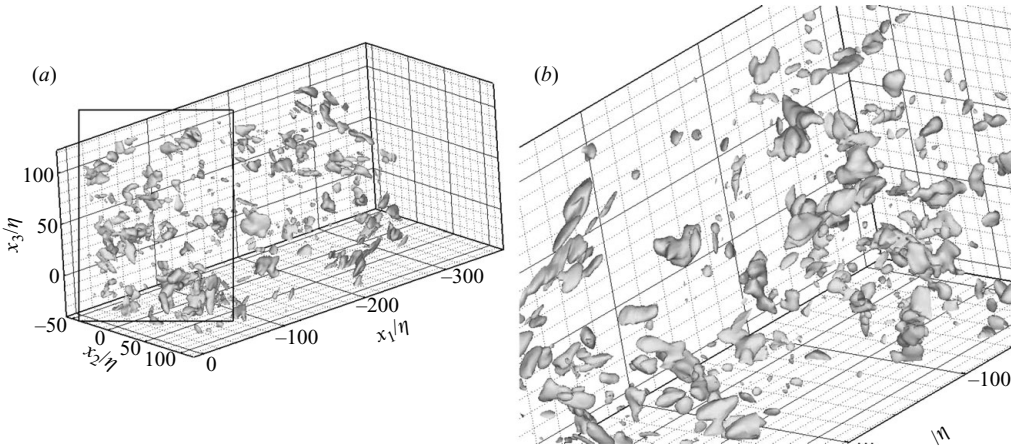


FIGURE 11. (a) Isosurfaces of enstrophy production rate, $\omega_i S_{ij} \omega_j = -1.5 \times 10^5 \text{ s}^{-3} = -0.36(v/\eta^2)^3$. (b) A close-up from a different perspective of the isosurfaces of $\omega_i S_{ij} \omega_j = -1.5 \times 10^5 \text{ s}^{-3}$ within the black rectangle shown in (a). Taylor's hypothesis was used to construct the volume from 200 instantaneous PIV frames. The axes are scaled by the Kolmogorov length scale, η .

it is assumed that fluid elements evolve according to the strain field that they are subjected to, it is reasonable to expect that an element subjected to two extensive strain rates for a period of time will be instantaneously 'sheet-like' and an element subjected to two compressive strain rates will be 'tube-like'. It should also be noted that the statistical results in § 3 are derived from point-wise statistics, whereas the visualizations presented in § 4 are finite objects. Nevertheless, figure 9 shows predominantly 'sheet-like' structures with a few 'tube-like' structures, which is consistent with the statistical results of figure 6. This is due to the fact that the statistical results are generated from exactly the same data as those used to generate the instantaneous visualizations.

By contrast, figure 11(a) shows that isosurfaces of strong vortex compression ($\omega_i S_{ij} \omega_j = -1.5 \times 10^5 \text{ s}^{-3} = -0.36(v/\eta^2)^3$) are 'spottier' than the vortex stretching isosurfaces of figure 9, where 'spotty' means displaying a spatial coherence over a much smaller scale in all directions. Again, this observation is reinforced by the different perspective of the same isosurfaces presented in figure 11(b). This instantaneous observation is also consistent with the statistical finding in figure 6(b) which shows that vortex compressing regions are a combination of weakly 'sheet-forming' and 'tube-forming' topologies.

Figure 12(a) shows intense swirling regions, in black ($\lambda_{ci} = 75 \text{ s}^{-1} = 3.55 \langle \lambda_{ci} \rangle$), together with the isosurfaces of intense vortex stretching regions from figure 9(a), in white. The figure clearly reveals the 'tube-like' nature of the high enstrophy, intensely swirling structures, consistent with other studies in the literature, for example Jiménez *et al.* (1993). The strongly swirling regions are situated within the regions of strong vortex stretching. However, the intense vortex stretching regions are not exclusive to the intense swirling regions. In fact, the vortex stretching regions do not just coincide with the swirling 'tubes/worms' but extend out into the areas surrounding the 'worms'. This instantaneous observation is again consistent with the statistical findings. Figure 5 shows that the more intensely vortex stretching regions exhibit an increasingly strong local swirling strength. The vortex stretching ($\omega_i S_{ij} \omega_j$) threshold value used to construct the visualizations of figure 9 is only exceeded by just under 2% of the total

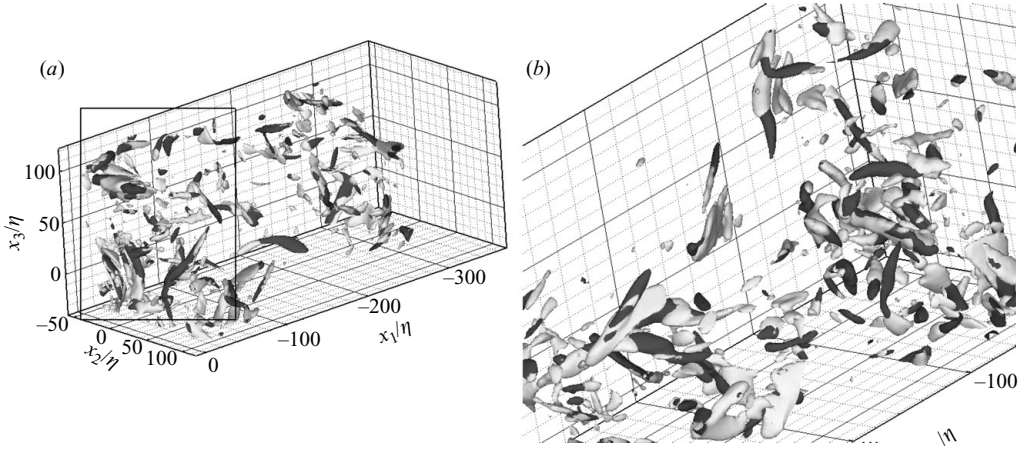


FIGURE 12. (a) Isosurfaces of $\omega_i S_{ij} \omega_j = 0.96(v/\eta^2)^3$ (white) and $\lambda_{ci} = 75 \text{ s}^{-1} = 3.55\langle\lambda_{ci}\rangle$ (black). (b) A close-up from a different perspective of the isosurfaces of $\omega_i S_{ij} \omega_j = 0.96(v/\eta^2)^3$ (white) and $\lambda_{ci} = 3.55\langle\lambda_{ci}\rangle$ (black) within the black rectangle shown in (a). Taylor's hypothesis was used to construct the volume from 200 instantaneous PIV frames. The axes are scaled by the Kolmogorov length scale, η .

volume, yet this accounts for 23 % of the total enstrophy production rate. Of these intensely vortex stretching regions, 86 % exhibit local swirling, of which the mean value is $2.40\langle\lambda_{ci}\rangle$. Figure 9, in conjunction with the statistical results, thus gives us a picture of intensely vortex stretching regions. These tend to be 'sheet-like' in nature and encompass the intensely swirling 'worms' that are extensively mentioned in the literature.

The literature also describes regions of strong dissipation as 'sheet-like' structures that surround the high enstrophy swirling 'worms' of figure 12, suggesting that they are likely to coincide with enstrophy producing regions. This can be observed in figure 13, which illustrates isosurfaces of intense kinetic energy dissipation ($\epsilon = 2.86(v^3/\eta^4)$) in black, and the isosurfaces of intense vortex stretching of figure 9, in white. The two sets of isosurfaces are observed to be in close proximity to each other from both the perspectives of figures 13(a) and 13(b). Again, this is consistent with the statistical results of figure 7 that shows that intensely vortex stretching regions also tend to be highly dissipative. This is not a surprising result. Regions of intense enstrophy production require a strong extensive strain field, as do dissipative regions since dissipation is a strain-related phenomenon. High enstrophy 'worms' induce such a strain field in their local surroundings encouraging vortex stretching. This is further backed up by figure 10(b) which shows a typical sheet of enstrophy production along with isosurfaces of $[A_{ij}]_+ = 1.43(v/\eta^2)^2$. This quantity picks out vortex sheets in which rotation and strain are of comparable magnitude, such as in the vortex sheets that surround high enstrophy 'worms'. The figure clearly shows that enstrophy production sheets tend to coincide with vortex sheets, which is a result that is consistent with the statistical findings presented in figure 8.

5. Conclusions

Cinematographic stereoscopic PIV data is used to examine the characteristics of enstrophy production by observing the alignment tendencies between the vorticity

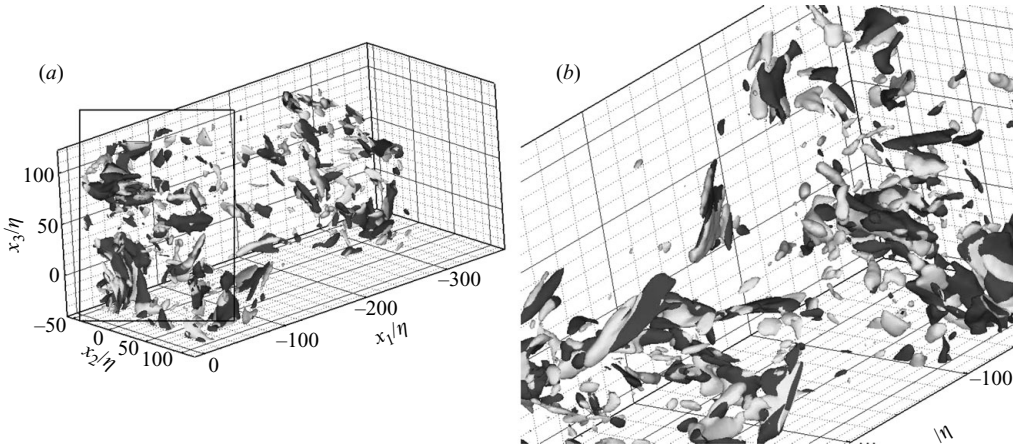


FIGURE 13. (a) Isosurfaces of $\omega_i S_{ij} \omega_j = 0.96(v/\eta^2)^3$ (white) and $\epsilon = 2.86(v^3/\eta^4)$ (black). (b) A close-up from a different perspective of the isosurfaces of $\omega_i S_{ij} \omega_j = 0.96(v/\eta^2)^3$ (white) and $\epsilon = 2.86(v^3/\eta^4)$ (black) within the black rectangle shown in (a). Taylor's hypothesis was used to construct the volume from 200 instantaneous PIV frames. The axes are scaled by the Kolmogorov length scale, η .

vector (ω) and the eigenvectors of the rate of strain tensor (e_i). The preferential alignment between the intermediate strain-rate eigenvector (e_2) and the vorticity vector, as reported extensively in the literature since the work of Ashurst *et al.* (1987), is confirmed. However, it is found that purely straining regions have a stronger alignment than swirling ones do. The alignment between ω and the intermediate and compressive strain-rate eigenvectors for swirling regions is more arbitrary than for straining regions. The p.d.f.s for the alignment between ω and e_1 are both flat indicating that the alignment between these two vectors is arbitrary, but in fact it is the 'average' of qualitatively different behaviour in enstrophy producing and enstrophy destroying regions.

Positive values of the enstrophy production rate, $\omega_i S_{ij} \omega_j$, are known to be favoured over negative ones (vortex compressing), and this is highlighted by the 'fatter' positive tail of the p.d.f. in figure 1. A joint p.d.f. was constructed between the second (Q) and third (R) invariants of the characteristic equation for the eigenvalues of D_{ij} , which is subsequently divided into four sectors defined by the sign of R and D , the discriminant of the characteristic equation. The sector for which $D > 0$ and $R < 0$ (S4) has a significantly greater mean enstrophy production rate than any of the other sectors. This sector is primarily comprised of strongly swirling regions, suggesting that although straining regions can be responsible for enstrophy production (S3), the highest enstrophy production rates are found in the presence of swirling. This finding is further supported by the joint p.d.f. in figure 5(a).

The alignment between ω and e_1 is observed to be of the greatest significance to the enstrophy production rate. Whilst the e_2 - ω alignment p.d.f.s for the four sectors of figure 3 are all qualitatively similar, those for the e_1 - ω alignment are fundamentally different. The p.d.f. for S1, for which the mean value of $\omega_i S_{ij} \omega_j$ is negative, shows that the vorticity vector is preferentially perpendicular to the extensive strain-rate eigenvector, whereas S3 and S4, for which $\omega_i S_{ij} \omega_j$ is positive, show the two vectors to be preferentially aligned. The p.d.f.s of figure 4 illustrate this fact, showing that negative values of $\omega_i S_{ij} \omega_j$ favour perpendicular alignment between

\mathbf{e}_1 and $\boldsymbol{\omega}$, whereas positive values of $\omega_i S_{ij} \omega_j$ favour parallel alignment between \mathbf{e}_1 and $\boldsymbol{\omega}$. It can thus be said that the flat p.d.f. for the overall alignment between \mathbf{e}_1 and $\boldsymbol{\omega}$ is the summation of the parallel alignment behaviour of enstrophy producing regions and the perpendicular alignment behaviour of enstrophy destroying regions.

Instantaneous visualizations of large $\omega_i S_{ij} \omega_j$ show that strong enstrophy producing regions are topologically ‘sheet-like’ and encompass the ‘tubes’/‘worms’ of intensely swirling high enstrophy structures. They extend into the surroundings of the high enstrophy ‘worms’ and hence also tend to be observed in close proximity to intensely dissipative regions, which have previously been shown to form ‘sheet-like’ structures that surround the high enstrophy ‘worms’ (Ganapathisubramani *et al.* 2008). This is backed up by the fact that enstrophy production regions are observed to coincide with the eigenvalue of the second-order velocity gradient tensor, $[A_{ij}]_+$, which identifies vortex sheets. All of these observations are consistent with the findings of the statistical results, which show a tendency for intensely enstrophy producing regions to be swirling and ‘sheet-forming’ due to their positive intermediate strain rate (s_2). By contrast, strong vortex compression regions tend to be ‘spotty’, with a less distinct structure. This is also in keeping with the statistical results, which show that vortex compression regions have no preference for positive or negative s_2 .

The authors would like to thank Professor N. T. Clemens for his support in granting permission to use the data and Professor J. C. Vassilicos for reading an internal version of the manuscript prior to submission. Funding from EPSRC is greatly appreciated.

REFERENCES

- ANDREOTTI, B. 1997 Studying Burgers’ models to investigate the physical meaning of the alignments statistically observed in turbulence. *Phys. Fluids* **9** (3), 735–742.
- ASHURST, W. T., KERSTEIN, A. R., KERR, R. M. & GIBSON, C. H. 1987 Alignment of vorticity and scalar gradient with strain rate in simulated Navier-Stokes turbulence. *Phys. Fluids* **30**, 2343–2353.
- BATCHELOR, G. K. & TOWNSEND, A. A. 1949 The nature of turbulent motions at large wave-numbers. *Proc. R. Soc. Lond. A* **199**, 238–255.
- BERMEJO-MORENO, I., PULLIN, D. I. & HORIUTI, K. 2009 Geometry of enstrophy and dissipation, resolution effects and proximity issues in turbulence. *J. Fluid Mech.* **620**, 121–166.
- BETCHOV, R. J. 1956 An inequality concerning the production of vorticity in isotropic turbulence. *J. Fluid Mech.* **1**, 497–504.
- BETCHOV, R. J. 1975 Numerical simulation of isotropic turbulence. *Phys. Fluids* **18** (10), 1230–1236.
- BUXTON, O. R. H. & GANAPATHISUBRAMANI, B. 2009 The classification and composition of fine scale eddies in a turbulent jet. In *47th AIAA Aerospace Sciences Meeting Including the New Horizons Forum and Aerospace Exposition*. *AIAA Paper* 2009-592.
- CHAKRABORTY, P., BALACHANDAR, S. & ADRIAN, R. J. 2005 On the relationships between local vortex identification schemes. *J. Fluid Mech.* **535**, 189–214.
- CHONG, M. S., PERRY, A. E. & CANTWELL, B. J. 1990 A general classification of three-dimensional flow fields. *Phys. Fluids A* **2** (5), 765–777.
- GANAPATHISUBRAMANI, B., LAKSHMINARASIMHAN, K. & CLEMENS, N. T. 2007 Determination of complete velocity gradient tensor by using cinematographic stereoscopic PIV in a turbulent jet. *Exp. Fluids* **42**, 923–939.
- GANAPATHISUBRAMANI, B., LAKSHMINARASIMHAN, K. & CLEMENS, N. T. 2008 Investigation of three-dimensional structure of fine-scales in a turbulent jet by using cinematographic stereoscopic PIV. *J. Fluid Mech.* **598**, 141–175.
- GULITSKI, G., KholmYANSKY, M., KINZELBACH, W., LÜTHI, B., TSINOBER, A. & YORISH, S. 2007 Velocity and temperature derivatives in high-Reynolds-number turbulent flows in the atmospheric surface layer. Part 1. Facilities, methods and some general results. *J. Fluid Mech.* **589**, 57–81.

- HAMLINGTON, P. E., SCHUMACHER, J. & DAHM, W. J. A. 2008 Direct assessment of vorticity alignment with local and non-local strain rates in turbulent flows. *Phys. Fluids* **20** (111703), 1–4.
- HORIUTI, K. 2001 A classification method for vortex sheet and tube structures in turbulent flows. *Phys. Fluids* **13** (12), 3756–3774.
- HORIUTI, K. 2003 Roles of non-aligned eigenvectors of strain-rate and subgrid-scale stress tensors in turbulence generation. *J. Fluid Mech.* **491**, 65–100.
- HORIUTI, K. & TAKAGI, Y. 2005 Identification method for vortex sheet structures in turbulent flows. *Phys. Fluids* **17** (121703), 1–4.
- JEONG, J. & HUSSAIN, F. 1995 On the identification of a vortex. *J. Fluid Mech.* **285**, 69–94.
- JIMÉNEZ, J. 1992 Kinematic alignment effects in turbulent flows. *Phys. Fluids A* **4** (4), 652–654.
- JIMÉNEZ, J., WRAY, A. A., SAFFMAN, P. G. & ROGALLO, R. S. 1993 The structure of intense vorticity in isotropic turbulence. *J. Fluid Mech.* **255**, 65–90.
- KERR, R. M. 1985 Higher-order derivative correlations and the alignment of small-scale structures in isotropic numerical turbulence. *J. Fluid Mech.* **153**, 31–58.
- KHOLMYANSKY, M., TSINOBER, A. & YORISH, S. 2001 Velocity derivatives in the atmospheric surface layer at $Re_\lambda = 10^4$. *Phys. Fluids* **13** (1), 311–314.
- KOLMOGOROV, A. N. 1962 A refinement of previous hypotheses concerning the local structure of turbulence in a viscous incompressible fluid at high Reynolds number. *J. Fluid Mech.* **13**, 82–85.
- MARTÍN, J., OOI, A., CHONG, M. S. & SORIA, J. 1998 Dynamics of the velocity gradient tensor invariants in isotropic turbulence. *Phys. Fluids* **10** (9), 2336–2346.
- MATSUDA, T. & SAKAKIBARA, J. 2005 On the vortical structure in a round jet. *Phys. Fluids* **17** (025106), 1–11.
- MORTON, B. R. 1984 The generation and decay of vorticity. *Geophys. Astrophys. Fluid Dyn.* **28**, 277–308.
- MULLIN, J. A. & DAHM, W. J. A. 2006 Dual-plane stereo particle image velocimetry measurements of velocity gradient tensor fields in turbulent shear flow. Part II. Experimental results. *Phys. Fluids* **18** (035102), 1–28.
- NOMURA, K. N. & POST, G. K. 1998 The structure and dynamics of vorticity and rate of strain in incompressible homogeneous turbulence. *J. Fluid Mech.* **377**, 65–97.
- PERRY, A. E. & CHONG, M. S. 1994 Topology of flow patterns in vortex motions and turbulence. *Appl. Sci. Res.* **53**, 357–374.
- RICHARDSON, L. F. 1926 Atmospheric diffusion shown on a distance-neighbour graph. *Proc. R. Soc. Lond. A* **110**, 709–737.
- RUETSCH, G. R. & MAXEY, M. R. 1991 Small-scale features of vorticity and passive scalar fields in homogeneous isotropic turbulence. *Phys. Fluids A* **3** (6), 1587–1597.
- SHE, Z. S., JACKSON, E. & ORSZANG, S. A. 1990 Intermittent vortex structures in homogeneous isotropic turbulence. *Nature* **344**, 226–228.
- SIGGIA, E. D. 1981 Numerical study of small-scale intermittency in three-dimensional turbulence. *J. Fluid Mech.* **107**, 375–406.
- DA SILVA, C. & PEREIRA, J. C. F. 2008 Invariants of the velocity-gradient, rate-of-strain, and rate-of-rotation tensors across the turbulent/nonturbulent interface in jets. *Phys. Fluids* **20** (055101), 1–18.
- SREENIVASAN, K. R. & ANTONIA, R. A. 1997 The phenomenology of small-scale turbulence. *Annu. Rev. Fluid Mech.* **29**, 435–472.
- TANAHASHI, M., IWASE, S. & MIYAUCHI, T. 2001 Appearance and alignment with strain rate of coherent fine scale eddies in turbulent mixing layer. *J. Turbulence* **2** (6), 1–17.
- TAO, B., KATZ, J. & MENEVEAU, C. 2002 Statistical geometry of subgrid-scale stresses determined from holographic particle image velocimetry measurements. *J. Fluid Mech.* **457**, 35–78.
- TAYLOR, G. I. 1938 Production and dissipation of vorticity in a turbulent fluid. *Proc. R. Soc. Lond. A* **164**, 15–23.
- TENNEKES, H. & LUMLEY, J. L. 1972 *A First Course in Turbulence*. MIT Press.
- TSINOBER, A. 1998 Is concentrated vorticity that important? *Eur. J. Mech. B. Fluids* **17** (4), 421–449.
- TSINOBER, A. 2000 Vortex stretching versus production of strain/dissipation. In *Turbulence Structure and Vortex Dynamics* (ed. J. C. R. Hunt & J. C. Vassilicos), pp. 164–191. Cambridge University Press.

- TSINOBER, A., KIT, E. & DRACOS, T. 1992 Experimental investigation of the field of velocity gradients in turbulent flows. *J. Fluid Mech.* **242**, 169–192.
- TSINOBER, A., ORTENBERG, M. & SHTILMAN, L. 1999 On depression of nonlinearity in turbulence. *Phys. Fluids* **11** (8), 2291–2297.
- TSINOBER, A., SHTILMAN, L. & VAISBURD, H. 1997 A study of properties of vortex stretching and enstrophy generation in numerical and laboratory turbulence. *Fluid Dyn. Res.* **21**, 477–494.
- TSURIKOV, M. 2003 Experimental investigation of the fine-scale structure in turbulent gas-phase jet flows. PhD thesis, University of Texas, Austin, USA.
- VINCENT, A. & MENEGUZZI, M. 1991 The spatial and statistical properties of homogenous turbulence. *J. Fluid Mech.* **225**, 1–20.
- VINCENT, A. & MENEGUZZI, M. 1994 The dynamics of vorticity tubes in homogeneous turbulence. *J. Fluid Mech.* **258**, 245–254.
- ZHANG, J., TAO, B. & KATZ, J. 1997 Turbulent flow measurement in a square duct with hybrid holographic PIV. *Exp. Fluids* **23**, 373–381.
- ZHOU, J., ADRIAN, R. J., BALACHANDAR, S. & KENDALL, T. M. 1999 Mechanisms for generating coherent packets of hairpin vortices in channel flow. *J. Fluid Mech.* **387**, 353–396.